Nanoscale Advances

ROYAL SOCIETY OF CHEMISTRY

PAPER

View Article Online
View Journal | View Issue

Cite this: *Nanoscale Adv.*, 2026, **8**, 2613

Morphology tailoring and improved electrochemical performance of hexagonal boron nitride (h-BN) for symmetric supercapacitor applications

Madhav Dobhal,[a] Aditya Sharma,*[a] Bhavi Agrawal,[a] Mayora Varshney,[b] Hyun-Joon Shin,*[c] Ranjeet Kumar Brajpuriya[a] and Shalendra Kumar[a]

Correlations among the crystal structure, electronic structure, morphology, and electrochemical performance of hexagonal boron nitride (h-BN) are a matter of debate and need systematic investigation of their implications for energy storage assets. This work explores the morphology-controlled synthesis of h-BN nanostructures and their influence on the structural, electronic, and electrochemical properties toward the development of a symmetric supercapacitor device. h-BN nanostructures were synthesized *via* a nitridation process at 900 °C using boric acid with urea, melamine, and a urea–melamine mixture as precursors. Scanning electron microscopy revealed that urea-derived h-BN exhibits a faceted and porous morphology, whereas the melamine-derived sample predominantly forms nanorod-like structures. X-ray diffraction (XRD) confirmed morphology-dependent changes in the XRD line shape and variations in the lattice parameters. X-ray photoelectron spectroscopy (XPS) results revealed σ-type sp^2 hybridization between B and N atoms in all the samples, while a higher sp^2/sp^3 ratio in the melamine-derived h-BN indicated reduced oxygen functionalization associated with the rod-like morphology. Electrochemical measurements, conducted in three-electrode configurations with 1 M KOH electrolyte, confirmed pseudocapacitive behaviour and delivered high specific capacitance values of 455.0 F g^{-1}, 516.8 F g^{-1}, and 493.3 F g^{-1} (at a scan rate of 2 mV s^{-1}) from the urea, melamine, and mixed-precursor-derived samples, respectively, highlighting morphology-dependent charge-storage characteristics. Furthermore, a symmetric supercapacitor assembled using nanorod-based h-BN electrodes in a Swagelok configuration delivered an energy density of 8.74 Wh kg^{-1} and a power density of 4500 W kg^{-1}, along with excellent cycling stability, retaining 77.1% of its initial capacitance after 10 000 charge–discharge cycles.

Received 7th January 2026
Accepted 6th March 2026

DOI: 10.1039/d6na00014b

rsc.li/nanoscale-advances

Introduction

The rapid expansion of the global population and economy has sharply increased energy demand. Although petroleum, coal, and natural gas remain the primary conventional energy sources, their limited availability, rising cost, and the emission of harmful gases such as CO and CO_2 have led to severe environmental degradation and accelerated global warming. To address these challenges, renewable energy technologies, including wind, solar, and hydropower, have substantially progressed. However, the intermittent and unpredictable nature of these sources limits their reliability, necessitating the development of other efficient and robust energy-storage technologies.[1,2] To meet modern energy requirements, lead-acid, nickel-ion, and lithium-ion batteries have been widely developed and commercialized. Although these batteries offer high voltage output and superior energy density, they suffer from drawbacks such as short cycle life, restricted power density, slow charge–discharge kinetics, and safety concerns.[3–6] Likewise, fuel-cell technologies provide high energy density, long cycling stability, low emissions, and flexible fuel options. Nevertheless, their high installation costs, complications associated with hydrogen storage, low power densities, and safety-related issues present substantial obstacles to large-scale practical deployment.[4–7]

In the context of energy storage, supercapacitors (SCs) have emerged as next-generation electrochemical energy storage devices that have earned significant appreciation due to their remarkable characteristics, such as high specific power (500–10000 W kg^{-1}), exceptional charging/discharging rate, longer

[a]*Department of Physics, SOAE, University of Petroleum and Energy Studies (UPES), Dehradun, Uttarakhand, 248007, India. E-mail: adityaiuac@gmail.com*
[b]*Department of Applied and Life Sciences, & Division of Research & Innovation, Uttaranchal University, Dehradun, Uttarakhand 248007, India*
[c]*Department of Physics, Chungbuk National University, Cheongju-28644, South Korea. E-mail: shin@chungbuk.ac.kr*

durability, and low maintenance cost. Structurally, they consist of two electrodes separated by an electrolyte and a separator. Supercapacitors are widely used in applications that require high power in shorter times, such as transportation. In recent years, they have drawn considerable interest in electric vehicles due to their fast charging capability. Furthermore, they have also found applications in low-power devices such as laptops and other portable electronics.[1,8–10] Based on the charge storage mechanism, SCs are characterized as electric double-layer capacitors (EDLCs), pseudocapacitors, and hybrid supercapacitors. The EDLCs are known for their high-power density, which makes them suitable for applications like power backup and regenerative braking systems; however, their energy density is lower (typically <5 Wh Kg^{-1}) compared to batteries.[11] In contrast, pseudocapacitors store energy *via* a faradaic reversible redox reaction at/or near the electrode surface. These materials include metal-oxides (MnO_2, RuO_2, V_2O_3, *etc.*) and conducting polymers (PANI and Ppy), which offer high specific capacity and high energy density (10–40 Wh kg^{-1}).[11] Hybrid supercapacitors are capable of providing a balanced approach for high energy and power density by merging features of the above two supercapacitors.[1,11–13]

Although several factors decide the performance of a supercapacitor device, the selection of electrode materials is one of the crucial factors. An ideal electrode should possess a high surface area, good chemical stability, and a large number of electrochemically active sites to facilitate rapid ion transport and efficient charge accumulation.[14,15] Porous carbonaceous materials, conducting polymers, and transition metal oxides (TMOs) are widely reported for developing high-performance supercapacitors.[16] However, the search for new and efficient materials remains a central focus for enhancing electrochemical performance and extending the lifespan of supercapacitors.

Among the several examined materials, two-dimensional (2D) materials have been identified as high-potential materials for supercapacitive energy storage. These materials include graphene,[16] reduced graphene oxide,[17] MXene,[17] graphitic carbon nitride (g-C_3N_4),[17] and hexagonal boron nitride (h-BN).[17] Such compounds exhibit significantly high surface area, excellent thermochemical stability, and tailorable compositions, which support easier charge transport pathways and increased accessibility of surface/active sites for improved charge storage performance.[16–20]

Among various explored 2D materials, hexagonal boron nitride (h-BN) has attracted extensive attention due to its structural resemblance to graphene and numerous unique features, such as high mechanical strength and exceptional resistance to chemical/thermal degradation, which make it highly suitable for energy storage applications.[11,20,21] Structurally, h-BN consists of an equal number of alternating nitrogen and boron atoms, arranged in a hexagonal honeycomb lattice. Across each plane, atoms are linked *via* strong covalent bonds formed through sp^2 hybridization, while adjacent planes are held together by weak van-der-Waals interaction.[21,22] h-BN is often termed "white graphite" due to its resemblance in structure to graphene, including interplanar distances, bond lengths, and the honeycomb lattice. In contrast to graphene, which exhibits purely covalent bonding, h-BN has partial ionicity due to electronegativity differences between B and N atoms, which, indeed, support pseudocapacitive behavior. The variations in oxidation states of boron and nitrogen during electrochemical reaction enable additional charge storage, while the nitrogen atoms further contribute by forming redox active sites, which leads to efficient charge transfer and high specific capacitance.[17,23] Furthermore, its high chemical stability and corrosion resistance ensure longer durability.[21,22] Altogether, the unique structural and electrochemical properties make h-BN a sustainable and high-performance electrode material with excellent specific capacitance, cycle stability, and durability for next-generation supercapacitors.

In past years, researchers have explored the electrochemical properties of h-BN in bare and composite forms. Li *et al.* reported a specific capacitance of 54.8 F g^{-1} at a current density of 0.5 A g^{-1} with 2 M KOH electrolyte, which improved to 250 F g^{-1} when combined with carbon (h-BN/C).[24] Maity *et al.* showed a low specific capacitance of ~33 F g^{-1} at a current density of 1 A g^{-1} for pristine h-BN, which could improve to 387.5 F g^{-1} with amalgamation with CNT and PANI (h-BN/CNT/PANI).[25] Dhamodharan K *et al.* reported a specific capacity of 68.3 C g^{-1} at 10 mV s^{-1} within a potential window of 0–0.6 V in 3 M KOH for bulk h-BN, which was further enhanced to 215.8 C g^{-1} at the same scan rate for exfoliated h-BN.[26] Prabhakar *et al.* reported a specific capacitance of 169.3 F g^{-1} at 1 A g^{-1} in 1 M KOH solution.[27] In such reports, h-BN could offer reasonable specific capacitance, but it experiences challenges in its single-phase formation.[28] Moreover, morphology tailoring and its implications for the structural, optical, electronic structure, and electrochemical properties are less investigated. Recent studies on other nanomaterials have demonstrated that controlled synthesis and morphology engineering can remarkably enhance material properties and performance.[29,30]

This study explores the morphology tailoring of h-BN by applying different precursors and incorporating additional synthesis protocols, compared to the existing literature.[3,31] The source of boron was kept the same (*i.e.*, boric acid; H_3BO_3), but the nitrogen-containing precursors (*i.e.*, urea; $(NH_2)_2CO$, and melamine; $C_3H_6N_6$) were bifurcated into different schemes of synthesis. The synthesized materials were thoroughly characterized to explore the effect of precursors on their morphology, crystal structure, optical properties, electronic structure, and electrochemical traits. Eventually, an optimized h-BN sample with better electrochemical traits was selected to prepare a symmetric supercapacitor device (Swagelok cell) with 1 M KOH electrolyte, which demonstrated a high energy density of 8.74 Wh kg^{-1} and a power density of 4500 W kg^{-1}. The device also offered good cycling stability, retaining 77.1% of its initial capacitance after 10 000 charge–discharge cycles.

Experimental details

Synthesis of h-BN

All reagents used were of analytical grade without any further purification. Boric acid (99.5% purity) and urea (99.5% purity)

were purchased from Molychem, India, and melamine (99.5% purity) was purchased from Srichem, India. h-BN was synthesized *via* three different routes, adapting the method from Mirzaee *et al.*,[31] with certain modifications. In the first route, stochiometric proportions of boric acid and urea were dissolved in deionized water (200 ml) and stirred for 2 h using a magnetic bead to ensure homogeneity. Likewise, in the second and third syntheses, boric acid and melamine, and boric acid and a mixture of urea and melamine were weighed in stoichiometric proportions and, separately, dissolved in deionized water (200 ml) with magnetic stirring for 2 h. The resultant solutions were, separately, dried overnight at 80 °C. The obtained powders were annealed at 900 °C in a tubular furnace under steady N_2 flow (0.05 L min^{-1}). The first-, second-, and third-route prepared samples are named h-BN(BU), h-BN(BM), and h-BN(BMU), respectively.

The nitrogen annealed samples were investigated with X-ray diffraction (XRD) for phase identification (see SI Fig. S1). Although h-BN was observed as the dominating phase, the XRD patterns exhibit a peak (near 15°) related to the boron oxide (B_2O_3) phase. This could be due to the development of residual B_2O_3 products during the reaction between the boron precursor and oxygen. This kind of impurity peak was also observed by Mirzaee *et al.*.[31] Therefore, to eliminate the impurity phase in the as-prepared samples, a systematic wiping process was employed. The above prepared samples were separately dispersed in anhydrous ethanol (50 ml), sonicated (for 10 min), air dried overnight, and heated at 80 °C for 5 h. Such dried samples were annealed at 900 °C for 4 h, with constant N_2 flow. An overall yield of ~60% was achieved after the purification process. The synthesis of h-BN is presented in Fig. S2 (SI). From the nature of synthesis and experimental findings, the plausible chemical reaction for the formation of h-BN from the constituent compounds can be written as:

For the urea and boric acid-based system:

$$2H_3BO_3 + 3CO(NH_2)_2 \rightarrow B_2O_3 + 3H_2O + 3NH_3 + 3NHCO$$

$$B_2O_3 + 2NH_3 \rightarrow 2BN + 3H_2O \quad (1)$$

For the melamine and boric acid-based system:

$$3H_3BO_3 + C_3H_6N_6 \rightarrow 3BN + 3CO_2 + 3H_2O + 3NH_3 \quad (2)$$

For urea, melamine, and boric acid-based systems:

$$H_3BO_3 + C_3H_6N_6 + 5CO(NH_2)_2 \rightarrow BN + 2CO_2 + 4H_2O + 5NH_3 + 6HCN + 2N_2 \quad (3)$$

Material characterization

The crystal structure and phase of the samples were examined using a Bruker D8 Advance EcoPro X-ray diffractometer with Cu Kα radiation (1.5405 Å). The functional groups in samples were analyzed by Fourier Transform infrared spectroscopy (FTIR) using a PerkinElmer FTIR spectrometer. Brunauer–Emmett–Teller (BET) analysis was conducted using an Anton Paar Autosorb 6100 FKM MP-AG instrument to determine the specific surface area and porosity. The surface morphology and elemental composition were analyzed by field emission scanning electron microscopy (FE-SEM) equipped with energy dispersive X-ray spectroscopy (EDS) using a JEOL JSM-7900F model. The chemical bonding was evaluated through lab source-based X-ray photoelectron spectroscopy (XPS) utilizing a Kratos Analytical AXIS SUPRA + machine. UV-visible absorption spectroscopy measurements were conducted using an RIMS UV/Vis spectrometer. Transmission electron microscopy (TEM) measurements were performed using a TALOS F200X machine.

Electrochemical measurements

The electrochemical performance of h-BN(BU), h-BN(BM), and h-BN(BMU) electrodes was assessed using a Corrtest instrument CS2350M electrochemical workstation. All measurements were carried out in a standard three-electrode configuration in which Ag/AgCl served as the reference electrode (RE), a platinum wire as the counter electrode (CE), and h-BN electrodes as the working electrodes (WEs) in an electrolyte of 1 M KOH aqueous solution. In order to prepare working electrodes, the nickel foam substrate (1 cm × 1 cm; 1.5 mm thick) was washed in ethanol, HCL, and DI water for 30 min each by using an ultrasonicator and dried at 80 °C overnight. After that, each h-BN sample, namely h-BN(BU), h-BN(BM), and h-BN(BMU), was individually combined with polyvinylidene fluoride (PVDF), and carbon black in an 8 : 1 : 1 ratio. The resultant was subsequently mixed with 3–4 drops of *N*-methyl-2-pyrrolidone (NMP) to make a slurry solution. The slurry was then deposited onto treated nickel foam using the drop cast method, followed by drying at 80 °C overnight. The dried electrodes were utilized as a working electrode for electrochemical analysis. The electrochemical characteristics of all three prepared h-BN samples were thoroughly investigated through cyclic voltammetry (CV), galvanostatic charge–discharge (GCD), and electrochemical impedance spectroscopy (EIS) using a standard three-electrode configuration. The CV measurements were performed in a potential range of 0.0 V–0.7 V with varying scan rates between 2 mV s^{-1} to 100 mV s^{-1}, whereas the GCD measurements were performed within the potential range of 0.0 V–0.5 V for different current densities.

The specific capacitance (C_{sp}) from CV was determined by using equation[33] $C_{sp} = \frac{\int I \cdot dV}{2 \cdot m \cdot \vartheta \cdot \Delta V}$, where $\int I \cdot dV$ is the area under the CV curve, m is the active material's mass loaded on Ni foam, ϑ is the scan rate, and ΔV is the applied potential difference. Also, the specific capacitance from the GCD graphs was evaluated using the relation $C_{sp} = \frac{I \cdot \Delta t}{m \cdot \Delta V}$. The energy density and power density were evaluated using the relations[33] $E = \frac{C \cdot \Delta V^2}{2}$ and $P = \frac{3600 \times E}{\Delta t}$, respectively,[33] where I denotes the applied current, 'Δt' is the discharge time, 'ΔV' is the potential window, and 'm' is the electrode mass. The energy

density and power density are measured in units of Wh Kg^{-1} and W Kg^{-1}, respectively. The analysis of solution resistance (R_s) and charge transfer resistance (R_{ct}) of all three samples was carried out using EIS in the frequency range of 0.1 Hz to 100 KHz.

A symmetric supercapacitor device was prepared using the h-BN (BM) sample. The electrodes were prepared by blending h-BN (BM), PVDF, and carbon black in an 8 : 1 : 1 ratio. The solvent NMP was used to make slurry solutions. The slurry was then deposited onto a graphitic paper substrate using the drop cast method and dried at 80 °C overnight. The electrochemical measurements of a supercapacitor device fabricated using a Swagelok cell and Whatman filter paper as a separator were carried out in a two-electrode configuration with 1 M KOH electrolyte. The specific capacitance of the symmetric device was evaluated from CV and GCD curves of the cell[32,33] using the relations[33] $C_{cell} = \frac{\int I \cdot dV}{m \cdot \vartheta \cdot \Delta V}$ and $C_{cell} = \frac{2 \times I \times \Delta t}{m \cdot \Delta V}$, respectively; here, $\int I \cdot dV$ is the area under the CV curve, m denotes the total mass loaded in both electrodes, ϑ is the scan rate, ΔV represents the voltage window, the applied current is denoted by I, and Δt denotes the discharge time. The energy density and power density of the cell were estimated using the relations[33,34] $E_{cell} = \frac{1}{4} \times 3.6\ C_{cell} V^2$ and $P_{cell} = \frac{E}{\Delta t} \times 3600$, respectively.

Results and discussion

XRD study

Fig. S3 shows the XRD patterns of h-BN samples and displays two intense peaks at ~26.0° and ~42.2°, corresponding to (002) and (100) crystal planes, respectively. These peaks fairly match with JCPDS card number- 96-591-0080 (space group, $P6_3/mmc$) and also match well with previous reports.[35,36] The Rietveld refinement was carried out, using FullProf software, to derive the structural parameters of the samples. A theoretical hexagonal crystal structure model of h-BN, as provided in the given JCPDS card, was used, and the fitted data are presented in Fig. 1(a) along with the experimental data, Bragg positions, and the difference between the experimental data and fitted data. It is noticeable that the fitted patterns match well with the experimental data and the Bragg positions of the (002) and (100) peaks also match, thus confirming the formation of h-BN products in all three syntheses. However, the XRD peak shape of the h-BN (BM) sample and fittings are slightly compromised compared to those of the other two samples. This could be due to the structural/morphological differences in this sample. The interplanar distance, lattice parameters, unit cell volume, crystallite size, and different r-factors and fitting parameters (χ^2, R_p, R_{wp}, and R_{exp}) are provided in Table S1. The evaluated lattice parameters and fitting parameters values are close to the reported values, strengthening the reasonably fitted results in this study.[35–37]

FTIR study

To understand the functional groups and their different vibrational behaviors associated with h-BN samples, systematic FTIR analysis was performed. Fig. 1(b) depicts the FTIR spectra and consists of several intense bands between 4000 cm^{-1} to 400 cm^{-1}. A broad absorption band at 3900 cm^{-1}–3370 cm^{-1} can be assigned to the stretching vibration modes of O–H or N–H groups.[36–38] Another strong absorption band is observed at 1300 cm^{-1}–1500 cm^{-1}, followed by low intensity absorption bands at 730 cm^{-1}–1000 cm^{-1}. The absorption bands at 740 cm^{-1}–1000 cm^{-1} can be assigned to the out-of-plane bending of sp^2 hybridized B–N networks (covalently connected B–N with some disorders). The absorption band at 1300 cm^{-1}–1500 cm^{-1} has been assigned to the in-plane stretching of sp^2 hybridized B–N networks.[35,39] Such vibrational bands have been reported as characteristic bands of h-BN and signify the formation of h-BN in all three samples.

UV-visible absorption spectroscopy study

The optical properties of synthesized h-BN samples were analyzed using UV-vis absorption spectroscopy and are presented in Fig. 1(c). All spectra exhibit strong absorption edges in the ultraviolet region, which is a characteristic feature of h-BN and arises from its wide band gap energy. Strong absorption peaks were observed at 243.8 nm, 247.3 nm, and 243.3 nm for h-BN(BU), h-BN(BM), and h-BN(BMU), respectively.

The optical band gap (E_g) energy for each sample was calculated using the Tauc equation,[40,41] $(\alpha h\upsilon)^2 = A(h\upsilon - E_g)$, where α is the absorption coefficient, $h\upsilon$ is the photon energy, A is a constant, and E_g is the optical band gap. The band gap values, obtained by extrapolating the linear regions of the $(\alpha h\upsilon)^2$ *vs.* $h\upsilon$ plots (Fig. 1(d)), were found to be 4.41 eV, 4.25 eV, and 4.40 eV for h-BN(BU), h-BN(BM), and h-BN(BMU), respectively. Hexagonal boron nitride (h-BN) is isostructural with highly oriented pyrolytic graphite; however, unlike graphite, it exhibits a semiconducting nature with a wide bandgap. Pristine h-BN typically possesses a bandgap of approximately 5.9 eV, which can be significantly modified by several factors, including the synthesis route, extrinsic doping, defects, and morphology changes.[40,41] The theoretical electronic band structure of h-BN was calculated using density functional theory (DFT).[40] Such results have demonstrated a direct bandgap located at the K point of the Brillouin zone and a band gap energy of 4.92 eV.[40] The DFT calculations indicated that the lower valence band (LVB) was predominantly contributed by N-s orbitals, with minor contributions from B-sp and N-p states. In contrast, the lower conduction band (LCB) was mainly governed by B-p orbitals, with comparatively smaller contributions from N-sp states. It has been reported that a rapid reduction in the bandgap energy takes place with decreasing interlayer distance.[40] In the present study, the XRD patterns have shown that h-BN (BU) and h-BN (BMU) samples have nearly the same $d_{(002)}$ spacing (~3.5 Å), but a net decrease in $d_{(002)}$ spacing (~3.4 Å) is observed for the h-BN (BM) sample. Therefore, it is anticipated that the smaller $d_{(002)}$ spacing values are responsible for the lower band-gap energy of the h-BN (BM) sample. Moreover, the smaller $d_{(002)}$ spacing values are analogous to the tight stacking of the h-BN networks, which originates from the higher degree of sp^2 hybridization (*i.e.*, strong σ bonds) in the sample.

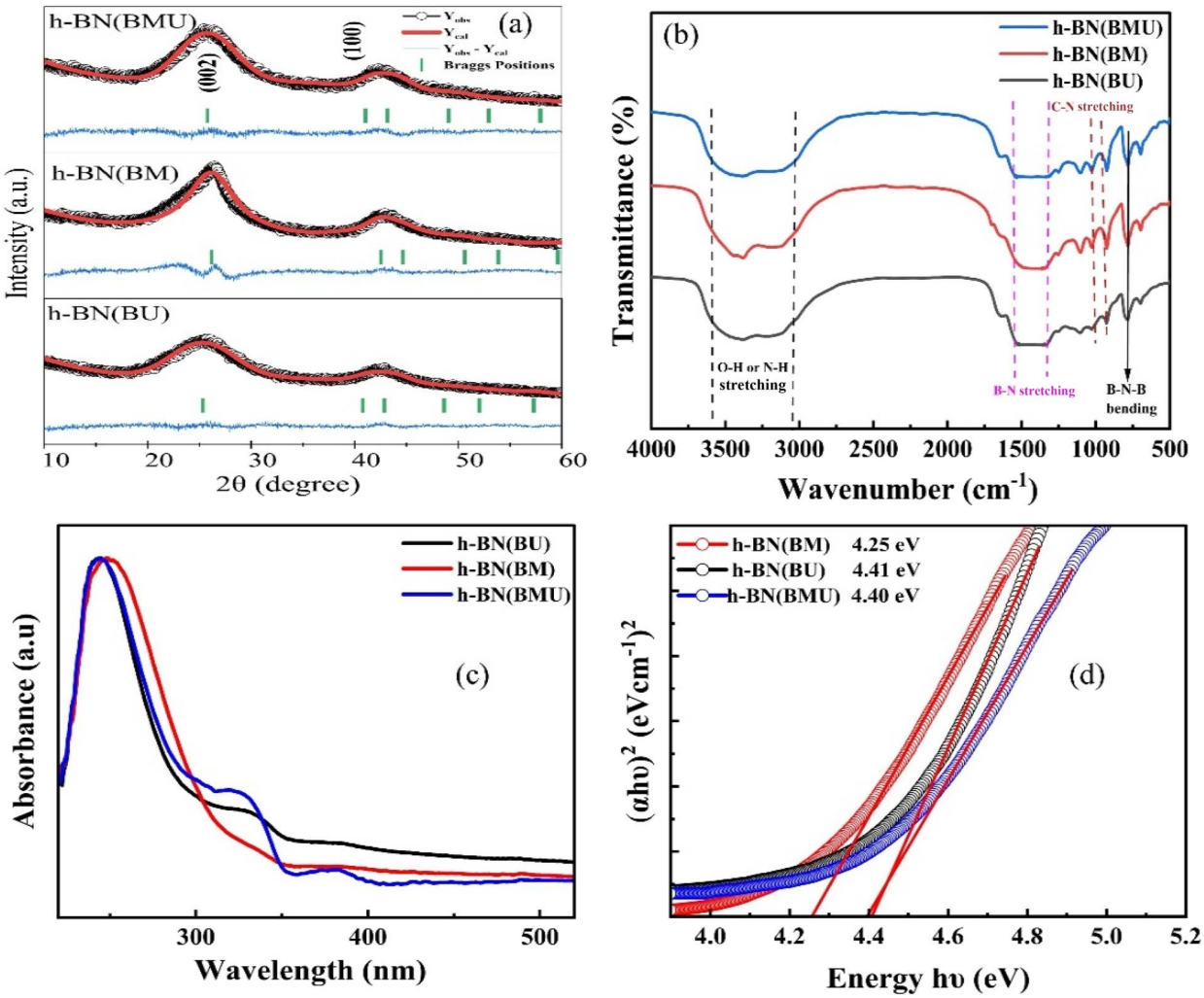

Fig. 1 (a) Rietveld fitted XRD patterns, (b) FTIR spectra, (c) UV-visible absorption spectra, and (d) Tauc plots of h-BN(BU), h-BN(BM), and h-BN(BMU) samples.

Thus, the smaller $d_{(002)}$ spacing (~3.4 Å) and narrower band-gap energy (4.25 eV) suggest a better degree of sp^2 hybridization in the h-BN (BM)sample.

FE-SEM and TEM results

To investigate the morphology variations in the samples, systematic FE-SEM and TEM measurements were performed and are depicted in Fig. 2. Fig. 2(a–c) shows the FE-SEM images and Fig. 2(d–f) shows the TEM images of h-BN(BU), h-BN(BM), and h-BN(BMU) samples, respectively. It is noticeable that the h-BN (BU) sample exhibits a porous morphology with some agglomerated sheets or pieces of material. On the other hand, an elongated rod-like morphology is observed for the h-BN (BM) sample. However, the h-BN(BMU) sample exhibits a somewhat dense or mended morphology. The EDS spectra (Fig. S4) of the three samples show dominant peaks of N and B along with the peaks from C and O. The N and B features are due to the h-BN materials, but C and O originate from the used carbon tape and adsorbed oxygen.

In a previous report, the sheet-like morphology has been reported from the urea-derived h-BN samples under isotropic growth.[31] However, anisotropic growth has been reported for the melamine-based precursors and resulted in the growth of nano whiskers, cauliflowers, and nanorod-like morphologies.[42,43] As per previous reports, the formation of rod-like or whisker morphology originates from anisotropic crystal growth driven by differences in the surface free energies of specific crystallographic planes.[42,43] This anisotropy is primarily associated with the (002) family of planes. The surface energies of the (002) and (004) planes were reported to be 18.32 and 6.55 kJ mol^{-1}, respectively.[44]

The significant difference in surface energies indicates preferential growth along the [001] direction, which exhibits a higher growth rate than other crystallographic directions. Consequently, the anisotropic growth promotes the formation of h-BN nanorods/nano whiskers oriented along the *c*-axis [0001].[45] Furthermore, planes possessing higher surface energies tend to grow more rapidly to minimize the total surface energy of the system. In this context, the (002) plane exhibits the

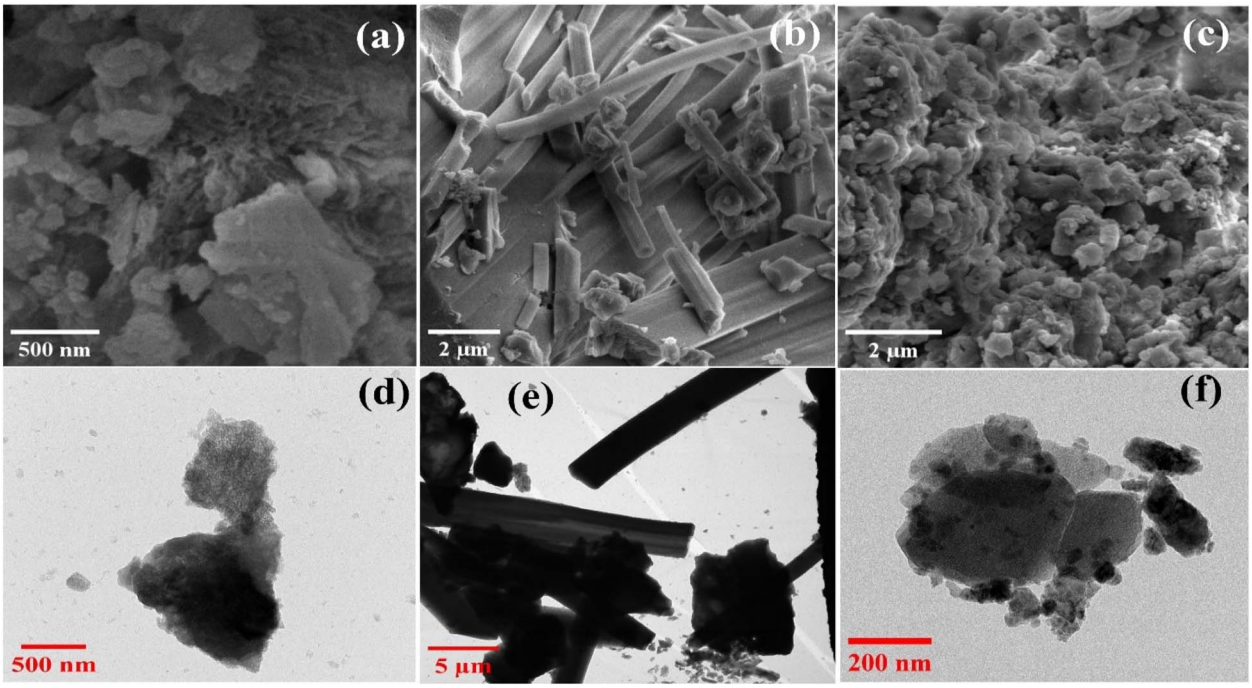

Fig. 2 FE-SEM images of (a) h-BN(BU), (b) h-BN(BM), and (c) h-BN(BMU). TEM images of (d) h-BN(BU), (e) h-BN(BM), and (f) h-BN(BMU).

maximum surface energy (3.186 J m^{-2}),[44] corroborating that the [0001] direction is the fastest growth direction. This preferential growth behaviour accounts for the observed rod-type morphology for the h-BN (BM) sample. Fig. 3 shows the mechanistic schematic of various kinds of morphology formation under the given synthesis protocols. First, the used precursors undergo hydrolysis (at 80 °C) and form various ions and smaller molecules.

Furthermore, with increasing annealing temperature, the initial building blocks of h-BN form for all the applied precursors. It is presented as h-BN nucleation. Depending on the used precursor, isotropic and anisotropic growth processes take place.[44–46] The cobbled sheet-like morphology is formed in the urea-based sample, driven by isotropic growth. On the other hand, a rod-like morphology is obtained in the melamine-based precursor due to anisotropic growth.[45] The mixture of precursors (urea and melamine) might involve competitive isotropic/anisotropic growth leading to a denser morphology.

XPS results

The chemical bonding (*i.e.*, sp^2 and/or sp^3 hybridization with their quantitative analysis) in the samples was investigated using XPS. Fig. 4(a) shows the XPS survey spectra of all three samples and exhibits B and N-related peaks from the h-BN compound. The C and O-related peaks are from the residual C and O in the samples. It is noticeable that the O content is much higher in the h-BN (BU) sample compared to the melamine-based samples (see the inset of Fig. 4(a)). HR-XPS spectra were also collected to estimate the different bonding among the constituent elements. The deconvoluted B1s and N 1 s spectra are presented in Fig. 4(b) and (c), respectively. The B 1s spectra exhibit prominent peaks at 190.83 eV (BU), 190.65 eV (BM), and 190.58 eV (BMU), which can be attributed to B–N bonding in h-BN. A slight variation in the peak position has also been reported in previous reports and assigned to the variations induced by different morphologies in the B–N bonding (*i.e.*, diverse attachment of B–N atoms in different morphologies).[47] Another peak, in the range 192.32–192.43 eV, is assigned to B–O bonding, which might arise due to attachment of oxygen moieties as residual oxygen from the reaction or atmospheric oxygen.[47]

The N 1s XPS spectra show a strong peak between 398.04–398.47 eV corresponding to the N–B bonding. The other peak at 400.02–400.30 eV, indicates N–H bonding. The N–H bonds are expected to form at the edge of the h-BN structure from –OH moieties or residual ammonia. The observed binding energies for synthesized h-BN samples were consistent with other reported XPS results for the same.[36,47] The main peak in the B 1s XPS (~190 eV) and/or the main peak in N 1s XPS (~398 eV) are related to sp^2 hybridization.[38,47] The higher energy peaks in N 1s and/or B 1s XPS spectra are due to defects or oxidation (or N–H kind of bonding) and represent sp^3 hybridization.[31,38,47] It is noticeable that the h-BN (BM) sample has a higher B–N/B–O bond ratio (*i.e.*, sp^2/sp^3 ratio) compared to the other two samples; these ratios were evaluated by estimating the area under the curve of XPS spectra and are presented in Table S2 and Fig. S5. This suggests that the melamine precursor helped to prevent oxygen moieties in the final product and led to the formation of dominant sp^2 hybridized B–B and/or N–N networks. The higher sp^2/sp^3 ratio for the h-BN (BM) sample may lead to tight stacking of h-BN groups, resulting in narrower

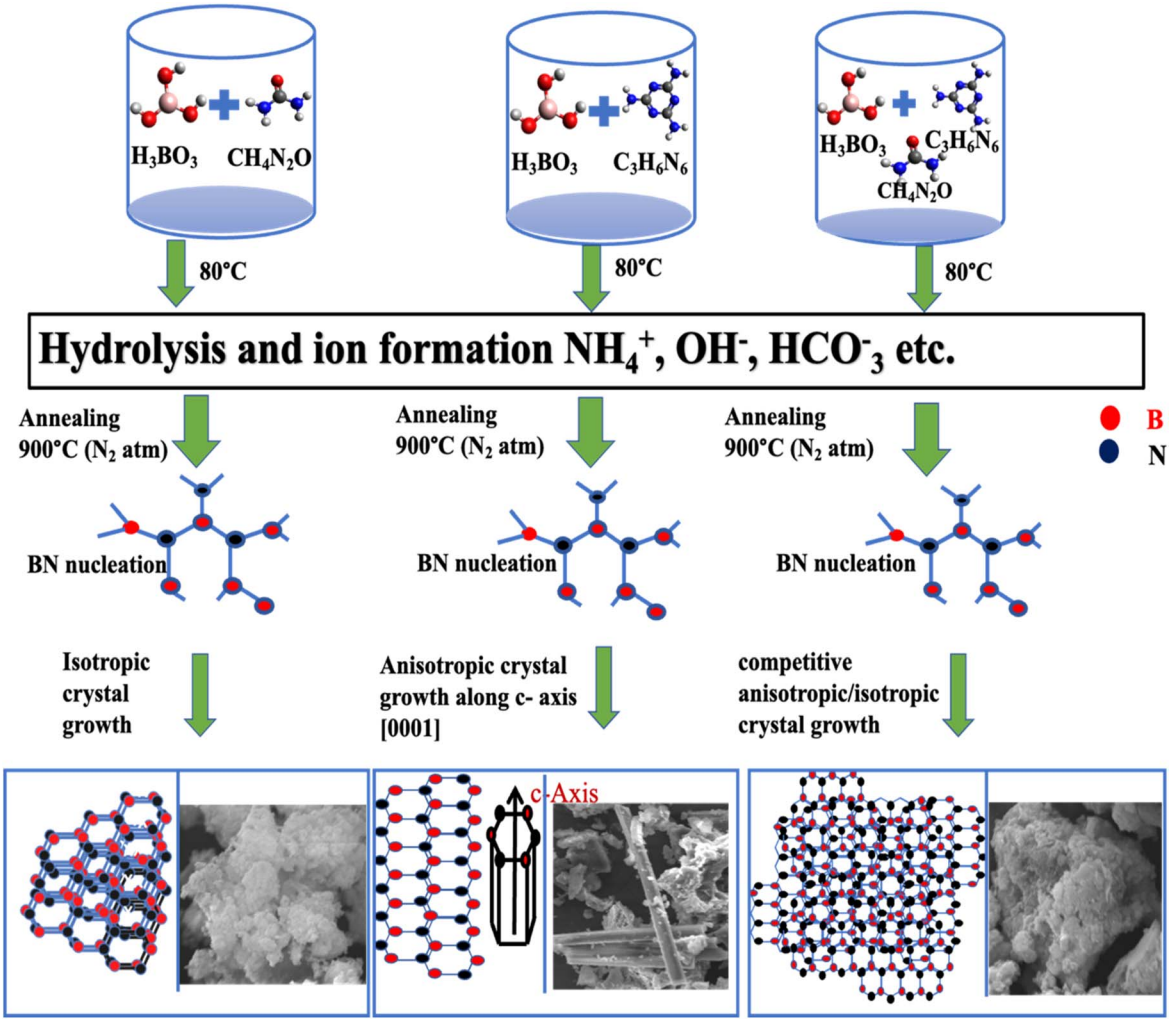

Fig. 3 Schematic of the growth of different morphologies of h-BN using different precursor batches.

$d_{(002)}$ spacing (as observed in the XRD results) and lower band-gap energy (as observed in the UV-vis spectroscopy investigations).

BET surface area results

Fig. S6(a) shows the nitrogen adsorption–desorption isotherms of the samples over a range of relative pressure ($P/P_0 = 0$ to 1). The sudden rise in adsorption–desorption at higher relative pressures indicates a type-III isotherm for all samples.[48] This can be attributed to the low surface energy and weak interactions between the adsorbate and the surface; as a result, the material facilitates multilayer adsorption instead of monolayer adsorption. Fig. S6(b) presents the pore size distribution curves calculated using the BJH method. All samples display a wide range of mesoporous structures, which can facilitate electrolyte access. The h-BN (BU) showed a specific surface area (SSA) of 5.45 $m^2 g^{-1}$ with an average pore diameter of 53.9 Å. The h-BN (BMU) sample showed an improved SSA of 29.24 $m^2 g^{-1}$ with an average pore diameter of 62.9 Å. In contrast, h-BN (BM) achieved a significantly higher SSA of 68.39 $m^2 g^{-1}$ with a large pore diameter of 160–400 Å.

This increased surface area may arise due to its elongated and less agglomerated rod-like morphology, as evidenced by the FE-SEM and TEM studies. The porosity observed in the synthesized h-BN samples may be attributed to gases released during precursor decomposition. Since each precursor decomposes at different temperatures and releases different amounts of gases, different pore structures are formed.[31,49]

Electrochemical investigations

The electrochemical measurements of h-BN (BU), h-BN (BM), and h-BN (BMU) electrodes were performed using a conventional three-electrode system using 1 M KOH electrolyte. The CV graphs of h-BN-based electrodes were studied in a voltage range of 0 V to +0.7 V with varying scan rates ranging from 2 mV s^{-1} to 100 mV s^{-1} and are presented in Fig. 5(a–d).

The cyclic voltammograms of h-BN electrodes exhibit significant oxidation and reduction peaks observed near 0.5 V and 0.24 V, respectively, demonstrating their pseudocapacitive behavior.[50]

Mechanistically, in the absence of an applied potential, K^+ and OH^- ions in the KOH electrolyte are randomly distributed.

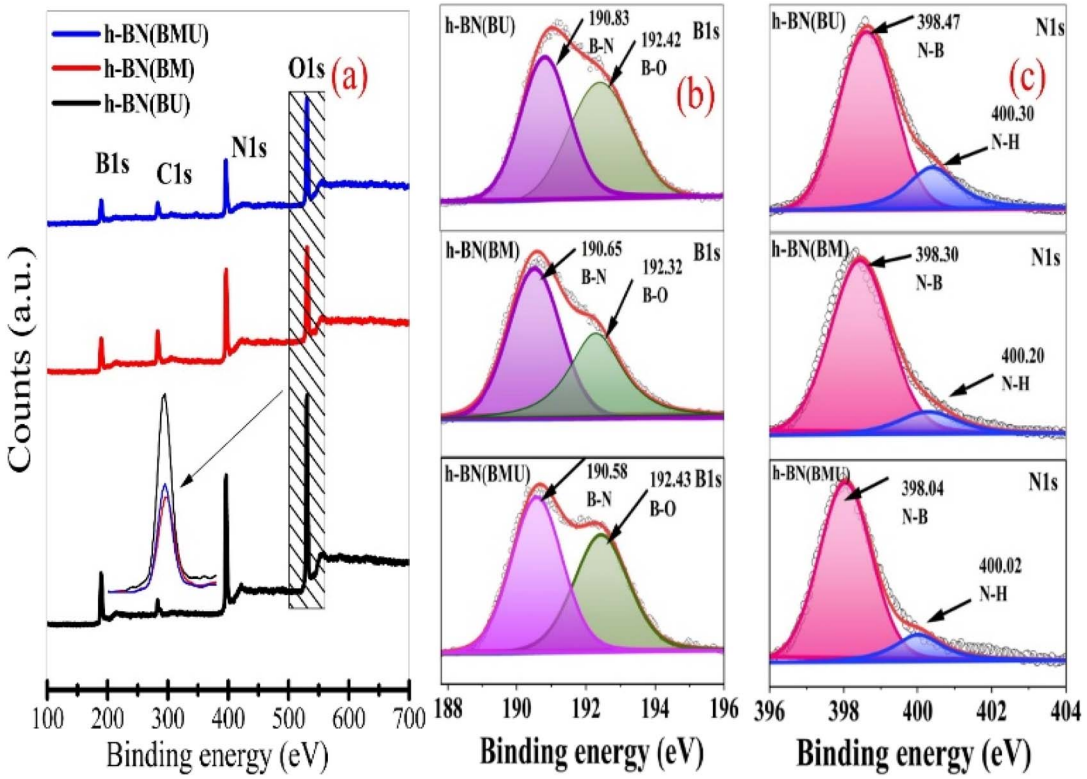

Fig. 4 (a) XPS survey spectra. High resolution XPS of (b) B 1s and (c) N 1s from h-BN (BU), h-BN (BM), and h-BN (BMU) samples.

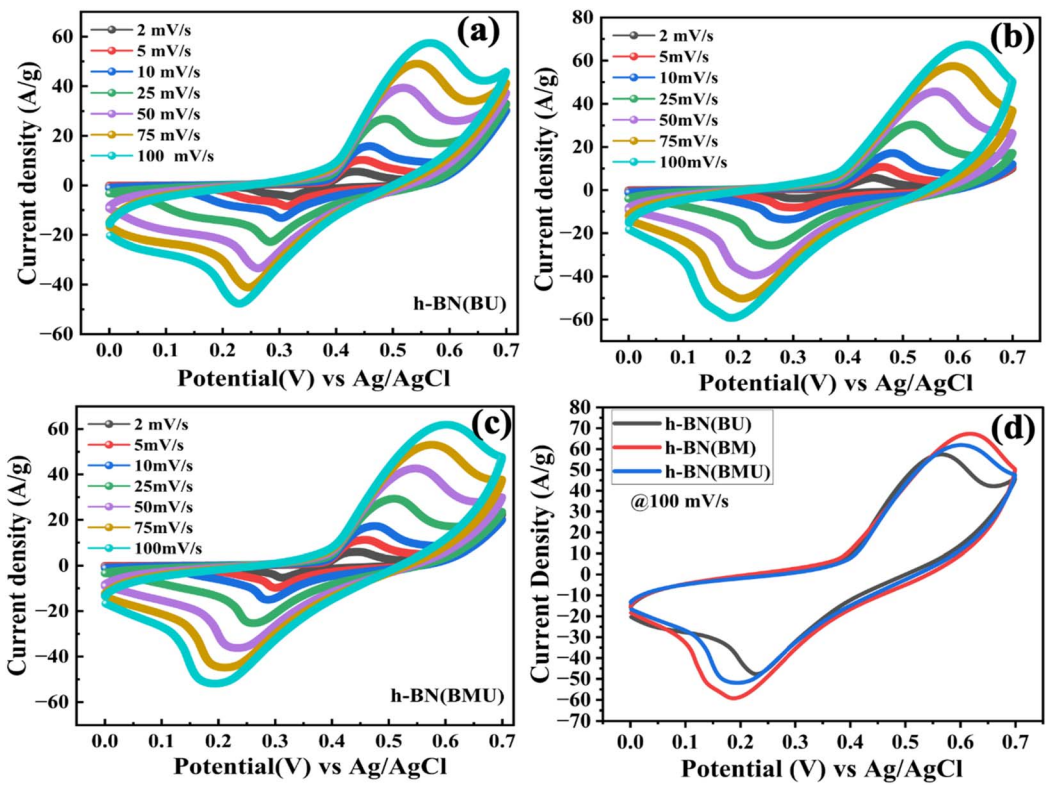

Fig. 5 CV characteristics, collected at different scan rates, of (a) h-BN(BU), (b) h-BN(BM), and (c) h-BN(BMU), and (d) comparison at 100 mV s^{-1}.

Upon applying a bias during cyclic voltammetry measurements, OH^- ions migrate toward the positively polarized h-BN working electrode. On the other hand, the K^+ ions move toward the negatively polarized region of the electrode–electrolyte interface, leading to the formation of an electric double layer that governs charge storage. The accessible surface area of h-BN nanostructures facilitates rapid ion adsorption and desorption, resulting in a capacitive current response. Charge neutrality in the system is maintained by the Pt counter electrode, where hydrogen evolution ($4H_2O + 4e^- \rightarrow 2H_2 + 4OH^-$) or oxygen evolution ($4OH^- \rightarrow O_2 + 4e^- + 2H_2O$) may occur depending on the applied polarization. During discharge, the applied potential is reversed, causing the collapse of the electric double layer at the h-BN/electrolyte interface. The adsorbed ions desorb back into the electrolyte, and electrons flow through the external circuit, releasing the stored energy. Throughout the process, the Ag/AgCl electrode provides a stable reference potential, ensuring accurate electrochemical characterization of the h-BN working electrodes. In the present case, for all samples, increasing the scan rate enhances the CV loop area and current density. This is because the current density, or simply current, is proportional to the scan rates ($i = C \cdot \upsilon$; υ is the scan rate, C is capacitance, and i is current). As the scan rate increases, the rate of potential change becomes faster, leading to a proportional increase in current response, thereby enlarging the CV loop area. It is noticeable from Fig. 5 that the current density of the h-BN (BM) sample is nearly 1.3 times higher than that of h-BN (BU) sample. This indicates better charge transport and storage in the h-BN (BM) sample. Fig. 5(d) shows the comparison of CV loops at a fixed scan rate (100 mV s^{-1}) and indicates better CV loops for the h-BN (BM) sample. The variation of specific capacitance with scan rate for all samples is listed in Table S3. In CV measurements, two major electrochemical processes take place at the electrode surface: the capacitive double layer formation and the diffusion-controlled faradaic reaction.[51] To examine the contributions from the two distinct charge storage processes, the relationship between anodic peak current (i) and scan rate (υ), based on the power-law equation ($i = a\upsilon^b$; $\log(i) = \log(a) + b\log(\upsilon)$), was analyzed by preparing $\log i$ *vs.* $\log \upsilon$ curves.[48,52] Here, a and b are arbitrary constants that quantitatively indicate the diffusion and adsorption/desorption (*i.e.*, surface) controlled capacitive nature of the samples. A b value of 1 indicates that the current linearly depends on the scan rate, resulting in a surface-controlled charge storage mechanism. On the other hand, $b = 0.5$ signifies proportionality of the current to the square root of the scan rate and diffusion-controlled charge storage mechanism in the samples.[48] The calculated b values for h-BN(BU), h-BN(BM), and h-BN(BMU) are presented in Fig. 6(a) and estimated to be 0.59, 0.63, and 0.62, respectively. This reveals that the charge storage mechanism of all three electrodes is primarily diffusion-controlled with a smaller contribution from surface-controlled processes. Among them, the h-BN(BM) electrode shows a slightly higher b-value (0.63), suggesting relatively enhanced surface activity and improved ion transport compared to the other two samples.

Furthermore, the total current density results from both surface-controlled ($k_1 \cdot \upsilon$) and diffusion-controlled ($k_2 \cdot \upsilon^{1/2}$) processes were calculated using relations, $\frac{i(V)}{\upsilon^{1/2}} = k_1 \cdot \upsilon^{1/2} + k_2$ and $i(V) = k_1 \cdot \upsilon + k_2 \cdot \upsilon^{1/2}$, respectively.[48,49] Based on these relations, the slope (k_1) and intercept (k_2) were obtained by plotting

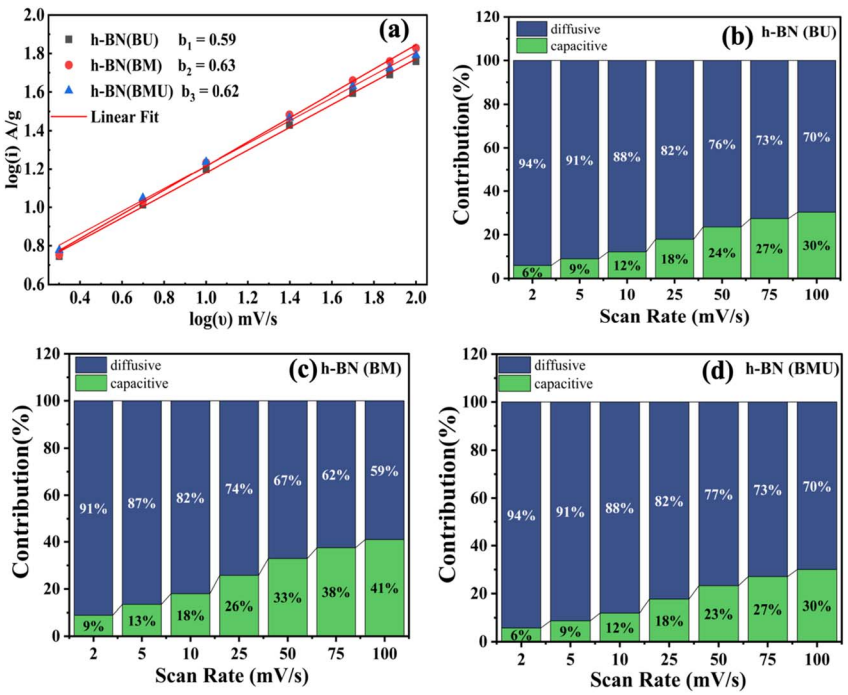

Fig. 6 (a) Comparison of $\log(i)$ *vs.* $\log(\upsilon)$ plots of h-BN(BU), h-BN(BM), and h-BN(BMU) samples. Capacitive and diffusive contribution plots of (b) h-BN(BU), (c) h-BN(BM), and (d) h-BN(BMU) samples.

$\frac{i(V)}{v^{1/2}}$ verses $v^{1/2}$.[53,54] Fig. 6(b–d) presents surface-controlled and diffusive-controlled current contributions to the total capacitance of h-BN electrodes. Likewise, for better visualization, the integrated CV loops (at a scan rate of 100 mV s^{-1}) for capacitive and diffusive contributions are provided in Fig. S6. At a scan rate of 2 mV s^{-1}, the surface-controlled contributions (green color in Fig. 6 and S7) were found to be 6%, 9%, and 6% for h-BN(BU), h-BN(BM), and h-BN(BMU), respectively, with the remaining fractions(94%, 91%, and 94%) corresponding to diffusion-controlled (blue color in Fig. 6 and S6) processes.

It is anticipated that K^+ ions may undergo adsorption/desorption from the electrolyte (KOH) onto the surface of h-BN nanostructures; $(h\text{-}BN)_{surface} + K^+ e^- \leftrightarrow (h\text{-}BN)^- - K^+$. Such adsorption/desorption kinetics contribute to significant charge storage in h-BN samples. However, the redox features in the CV curves indicate oxidation/reduction-based capacitive behavior in the h-BN samples. Typically, h-BN exhibits minimal to no intrinsic oxidation or reduction reactions (redox peaks) within a typical electrochemical window.[45] However, the native defects and oxygen-containing functional groups (as evidenced from the XPS results), which introduce interlocking defective hexagonal rings in h-BN, may facilitate oxidation/reduction reactions. The plausible oxidation reaction of h-BN, in alkaline media, may involve the development of nitrogen-based oxides (at the defective rings with non-bonding N atoms) through the following reaction: $h\text{-}BN + xOH^- \rightarrow h\text{-}BN(O)x + xe^- + xH_2O$. On the other hand, the reduction reaction may involve electron uptake which causes the formation of nitrogen species with a lower oxidation state; $h\text{-}BN(O)x + xe^- + xH_2O \rightarrow h\text{-}BN + xOH^-$. In the case of urea-based h-BN samples, typical agglomerated sheets or faceted morphologies have been observed, which may not have distinct surface/edges for adsorption/desorption kinetics, leading to lower surface-controlled contributions to the capacitance (Fig. 6(b–d) and S7).

The h-BN(BM) sample has a distinct rod-like morphology, higher sp^2/sp^3 ratios, and a larger surface area. Thus, it exhibits better surface-related specific capacitance. On the other hand, better diffusion of ions is expected in the typical agglomerated/porous sheets or faceted morphologies. Therefore, diffusion-based capacitance contribution is higher in the h-BN (BU) and h-BN(BMU) samples.

Along with cyclic voltammograms, the electrochemical performance of the electrode materials was investigated using GCD and is presented in Fig. 7, measured at current densities ranging from 1 A g^{-1} to 10 A g^{-1} within a voltage range of 0 V to +0.5 V. The asymmetric type charging/discharging characteristics observed in the GCD curves also confirm the pseudocapacitive behavior of h-BN samples.[49,55] It is noticeable that at a lower current density (1 A g^{-1}) all the samples exhibit nearly the same discharging characteristics (up to ~500 s). Distinct differences were seen when the current densities were elevated (2 A g^{-1} and higher). A comparison of charging/discharging times, at 2 A g^{-1}, is presented in the inset of Fig. 7(d). The h-BN (BM) sample exhibits a longer discharge time than the other two samples. In all samples, the charge–discharge times

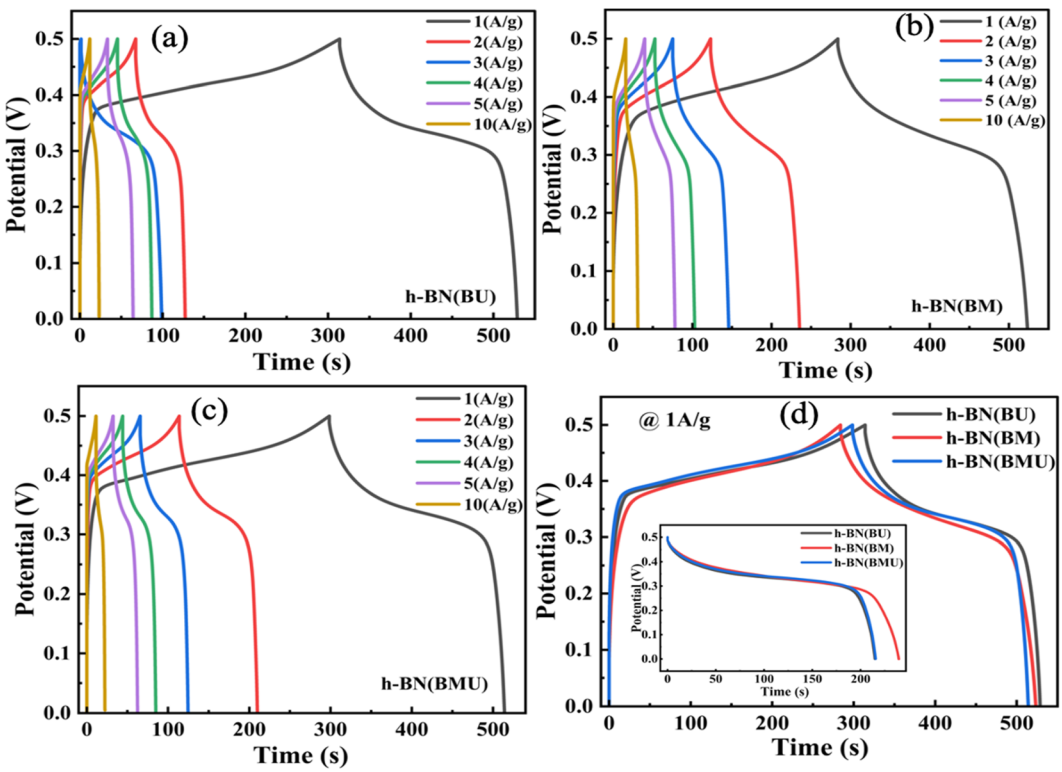

Fig. 7 GCD results, collected at different current densities, of (a) h-BN(BU), (b) h-BN(BM), and (c) h-BN(BMU). (d) Comparison of GCD at 1 A g^{-1}. The inset image shows discharge time comparison at 2 A g^{-1}.

decreased with increasing current density due to rapid ion transport and limited access to active sites. The discharge profiles exhibited an initial internal resistance drop, followed by a linear region characteristic of electric double-layer capacitance, and a subsequent sloped region indicating pseudocapacitive behaviour.[51] It is also noticeable that the potential window of all h-BN samples is the same, but the h-BN (BM) sample exhibits a longer discharge time than the other two samples, which is an exciting characteristic for its practical applications. The variation in the specific capacitance values at different current densities is listed in Table S4.

To further understand the electrochemical behavior of the electrodes, the EIS measurements were performed within the frequency range of 0.1 Hz to 100 kHz. The Nyquist plots of h-BN(BU), h-BN(BM), and h-BN(BMU) electrodes, along with their equivalent circuit/curve fitting, are shown in Fig. 8. The EIS data from individual samples are provided in Fig. S8. The overall impedance behaviour of the electrode can be understood using three key parameters. The first one is the series resistance (R_s), which represents the combined resistance arising from the electrode material, the electrolyte, and the contact interface between the active material and the current collector. In the Nyquist plot, R_s is determined from the first intercept of the semicircle with the real (x) axis. The second parameter, charge transfer resistance (R_{ct}), reflects the resistance encountered during charge transfer at the electrode–electrolyte interface. In the impedance spectrum, R_{ct} is represented by the diameter of the semicircle. A smaller diameter indicates a lower R_{ct} value and, consequently, more efficient charge transfer. The deviation from an ideal vertical line in the low-frequency region of the EIS curve is associated with the Warburg impedance element, described by $W = A/(j\omega)^{1/2}$, where A denotes the Warburg coefficient and ω is the angular frequency. This component occurs due to ion diffusion in the electrolyte, which becomes frequency dependent at lower frequencies (ω < 0.1 Hz). All three plots exhibit a negligible semicircular arc in the high frequency region, followed by a slanted line in the low frequency region. The high frequency region of the Nyquist plot represents the solution resistance (R_s) at the electrode/electrolyte interface, while the low frequency region corresponds to the charge transfer resistance (R_{ct}), which is developed at the electrode surface. The negligible semicircular arc in the high frequency region indicates excellent electrical conductivity and minimal internal and surface resistance.[33,56] The equivalent circuit (inset, Fig. 8), comprising R_s, R_{ct}, double-layer capacitance (C), and Warburg impedance (W_s) parameters, was used to fit the experimental data. The obtained R_s values for h-BN(BU), h-BN(BM), and h-BN(BMU) were 2.838 Ω, 2.409 Ω, and 2.505 Ω, respectively. Lower R_s and R_{ct} values indicate good conductivity and better charge transport in h-BN samples.

Specific capacitance values were evaluated from the CV and GCD data and are presented in Fig. 9(a) and (b). Fig. 9(a) displays the results of specific capacity *vs.* scan rate. The calculated specific capacitance values, at a scan rate of 2 mV s^{-1}, are 455.0 F g^{-1}, 516 F g^{-1}, and 493.3 F g^{-1} for h-BN(BU), h-BN(BM), and h-BN(BMU) samples, respectively. Likewise, Fig. 9(b) shows the current density *vs.* specific capacitance graph and exhibits values of 429.5 F g^{-1}, 479.2 F g^{-1}, and 431.3 F g^{-1}, at a current density of 1 A g^{-1}, for h-BN(BU), h-BN(BM), and h-BN(BMU) samples, respectively. These results show that the h-BN (BM) sample exhibits superior specific capacitance over the other two samples. Moreover, it is noticeable that specific capacitance decreases with increasing scan rates or current density. Typically, at lower scan rates or low current

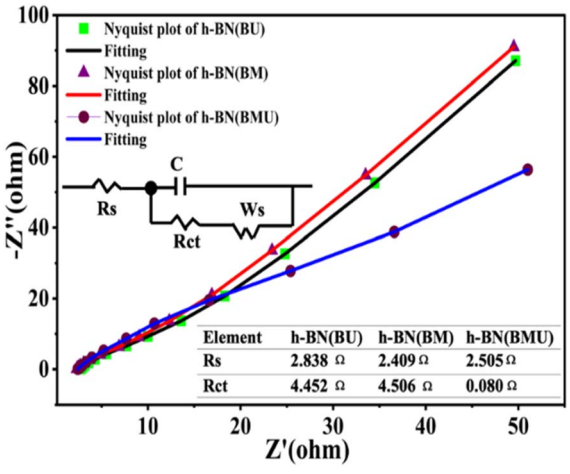

Fig. 8 Nyquist plots, along with fitting curves and equivalent circuit diagrams, of h-BN(BU), h-BN(BM), and h-BN(BMU). The series resistance (R_s), and charge transfer resistance (R_{ct}) values are provided for each sample.

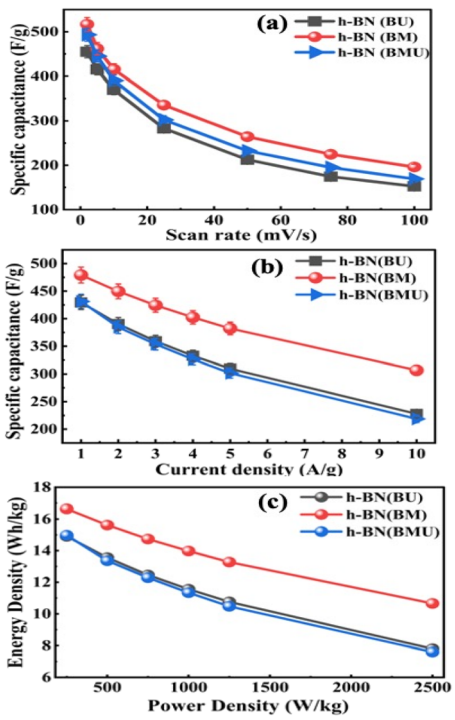

Fig. 9 (a) Specific capacitance *vs.* scan rate. (b) Specific capacitance *vs.* current density. (c) Ragone plots for h-BN(BU), h-BN(BM), and h-BN(BMU) samples.

density, electrolyte ions get enough time to penetrate the interior of the electrode material, enabling enhanced ion–electrode interaction and higher specific capacitance. In contrast, at higher scan rates or higher current density, limited ion diffusion into the bulk of the material restricts charge storage. Thus, the reduced rate of ion penetration leads to lower specific capacitance at higher current density. The energy density and power density of h-BN electrodes are also evaluated from GCD data of the samples. The Ragone plot (energy density *vs.* power density) is shown in Fig. 9(c). The obtained maximum energy and power densities of the h-BN (BU) electrode are 14.91 Wh kg^{-1} and 2500 W kg^{-1}. In the case of h-BN (BMU), the maximum energy and power densities were 14.98 Wh kg^{-1} and 2500 W Kg^{-1}, respectively. The highest energy density of 16.64 Wh kg^{-1} and a power density of 2500 W Kg^{-1} have been achieved for h-BN (BM) samples. In the present study, even at the maximum scan rate (100 mV s^{-1}) or maximum current density (10 A g^{-1}), the observed specific capacitance is ~150 F g^{-1} or ~200 F g^{-1}, which is far better than those of many of the oxides (*e.g.*, SnO_2, ZnO, CeO_2, *etc.*) or 2D (*e.g.*, g-C_3N_4) materials.[57] Likewise, the energy density and power density are superior to those of many of the previously reported 1D/2D materials.[45,58]

h-BN (BM) based symmetric supercapacitor device testing

By considering the elevated specific capacitance and energy density values of the h-BN(BM) sample, a symmetric supercapacitor device was fabricated in a two-electrode Swagelok cell configuration. The device performance was evaluated through CV, GCD, EIS, cycle stability, and practical LED demonstration. Fig. 10(a) displays the CV responses of the device, measured at different scan rates ranging from 2 mV s^{-1} to 100 mV s^{-1} within a potential window of 0–1.8 V. The CV curves exhibit a quasi-rectangular shape with redox peaks indicating combined capacitive and pseudocapacitive behavior.[55] The specific capacitance values are 73.10 F g^{-1}, 54.19 F g^{-1}, 42.70 F g^{-1}, 30.55 F g^{-1}, 23.63 F g^{-1}, 20.56 F g^{-1} and 18.90 F g^{-1} at 2 mV s^{-1}, 5 mV s^{-1}, 10 mV s^{-1}, 25 mV s^{-1}, 50 mV s^{-1}, 75 mV s^{-1} and 100 mV s^{-1}, respectively. Likewise, GCD data were collected in the same potential range of 0–1.8 V at various current densities ranging from 0.5 A g^{-1} to 5 A g^{-1} and are presented in Fig. 10(b). The specific capacitance values obtained from GCD are 38.83 F g^{-1}, 26.67 F g^{-1}, 16.44 F g^{-1}, 12.00 F g^{-1}, 9.16 F g^{-1} and 7.11 F g^{-1} at 0.5 A g^{-1}, 1 A g^{-1}, 2 A g^{-1}, 3 A g^{-1}, 4 A g^{-1} and 5 A g^{-1} respectively. These results demonstrate that the device maintains appreciable capacitance even at higher current densities, such as 5 A g^{-1}. The fabricated device was subjected to 10 000 continuous charge–discharge cycles at a current density of 4 A g^{-1}, and the results are presented in Fig. 10(c), which also includes the schematic illustration of Swagelok cell construction (inset image). After 10 000 cycles, the device retains 77.1% of its initial capacitance, reflecting excellent durability and structural stability under continuous charge–discharge operation. EIS was employed to evaluate the ion transport behavior of the h-BN-based symmetric supercapacitor, and the data are presented in Fig. 10(d), where the Nyquist plots before and after cycling are fitted using an equivalent circuit model (inset image). The fitted parameters reveal that the series resistance (R_{esr}) increased slightly from 1.004 Ω (before cycles) to 1.113 Ω (after cycles), while the charge transfer resistance (R_{ct}) decreased slightly from 2.778 Ω to 2.581 Ω. This displays a negligible change in impedance characteristics of the device after 10 000 cycles, suggesting that the electrode–electrolyte

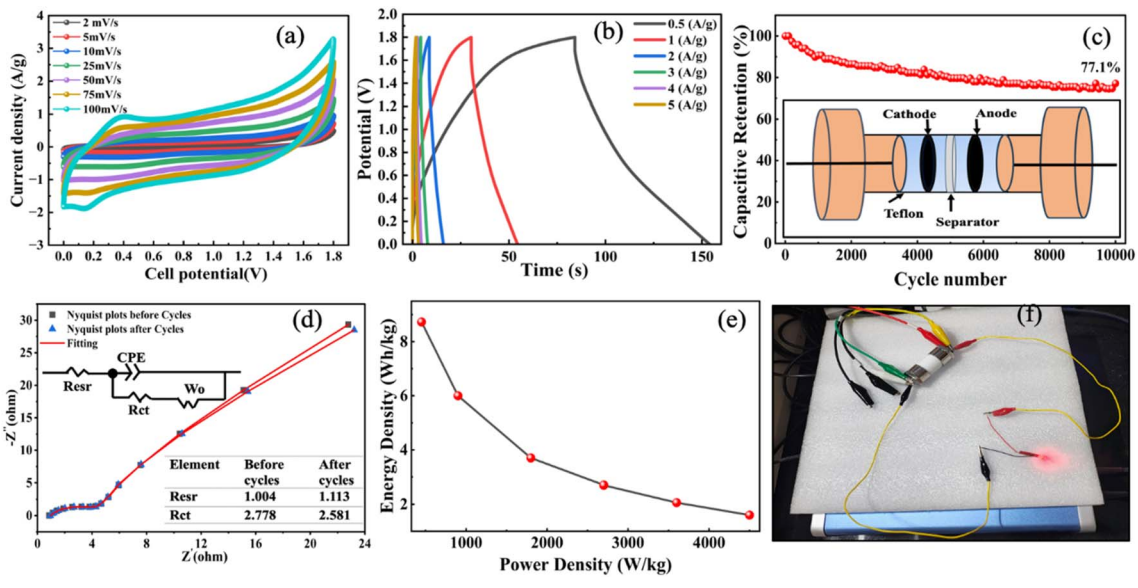

Fig. 10 (a) CV graphs of the h-BN(BM) based symmetric supercapacitor at different scan rates, (b) GCD characteristics of the h-BN(BM) based symmetric supercapacitor device measured at different current densities, (c) cycle performance of the h-BN(BM) based symmetric supercapacitor over 10 000 cycles, (d) Nyquist plots of the h-BN(BM) based symmetric supercapacitor device (collected before and after 10 000 cycles), (e) Ragone plot of the h-BN(BM) based symmetric supercapacitor, and (f) the real time picture of a red LED illuminated by the h-BN(BM) based symmetric supercapacitor.

interface remains stable with minimal degradation. The Ragone plot of the Swagelok cell device is presented in Fig. 10(e). The energy density (E_{Cell}) and power density (P_{Cell}) were estimated and found to be 8.74 Wh kg^{-1} and 4500 W kg^{-1}, respectively. To evaluate the practical performance of the fabricated device, the symmetric supercapacitor was applied to power a red LED, which illuminated successfully, as shown in Fig. 10(f). Overall the symmetric supercapacitor device showed notable specific capacitance, energy, and power densities along with cycle stability and reliable practical performance.

Post-cycle testing of electrodes for structural and morphology analysis

To further examine the structural stability and surface integrity of the h-BN electrode, after prolonged electrochemical cycling, XRD and SEM investigations were performed on the h-BN (BM) device electrode. Fig. S9 shows the XRD pattern of the post-cycled h-BN electrode. The characteristic diffraction peak near $2\theta \approx 26°$ corresponds to the (002) plane of h-BN, overlapping with the dominant XRD peak of graphitic paper. The other XRD peak, near 42°, is from the (100) plane of h-BN. The peak around 55° mainly originates from the graphitic substrate. Fig. S10 shows post-cycle SEM images of the h-BN (BM) electrode. This indicates that the morphology of the h-BN (BM) sample-based electrode remains stable and exhibits significant attachment between the h-BN (BM) rods and the graphitic substrate. This suggests good mechanical stability even after prolonged electrochemical operation. Although some small cracks and voids can be seen on the surface, these are likely formed due to continuous ion insertion and extraction of ions during the cycling process. However, there is no evidence of major morphological damage. Furthermore, the EDS results show clear peaks of boron and nitrogen, confirming the presence of h-BN. Carbon is detected from the graphitic substrate, while the small oxygen signal may be due to surface oxidation. Potassium peaks in the EDS spectrum likely arise from residual electrolyte.

Conclusions

In conclusion, this study demonstrates a morphology-controlled strategy for tailoring the structural, electronic, and electrochemical properties of hexagonal boron nitride (h-BN) nanostructures for high-performance supercapacitor applications. h-BN was successfully synthesized *via* a high-temperature nitridation route using different (urea, melamine, and their combination) nitrogen-rich precursors, leading to distinct nanostructured morphologies. Structural characterization confirmed the formation of crystalline h-BN, with morphology-dependent variations in diffraction line shapes and lattice parameters, underscoring the influence of precursor chemistry on crystal growth. XPS analysis revealed dominant σ-type sp^2 hybridization between boron and nitrogen atoms, while the higher B–N/B–O bond ratio (or sp^2/sp^3 ratio) observed in melamine-derived h-BN indicates reduced oxygen functionalization associated with the nanorod-like morphology. The strong σ type sp^2 dominated hybridization between B and N atoms leads to a narrower interplanar spacing of the (002) plane and contributes to a reduction in band-gap energy. Electrochemical investigations in a three-electrode configuration using 1 M KOH electrolyte established clear morphology-dependent pseudocapacitive behaviour. Among the synthesized samples, nanorod-based h-BN exhibited superior charge-storage performance, delivering a high specific capacitance of 516.8 F g^{-1} at a scan rate of 2 mV s^{-1}. The enhanced electrochemical response is attributed to an improved electronic structure, reduced oxygen-related defects, and favourable ion-accessible pathways arising from the nanorod architecture. Furthermore, a symmetric supercapacitor device fabricated using the optimized h-BN electrode delivered an energy density of 8.74 Wh kg^{-1} and a power density of 4500 W kg^{-1}, along with excellent cycling durability, retaining 77.1% of its initial capacitance after 10 000 charge–discharge cycles. The successful demonstration of LED illumination further validates the practical viability of the device.

Author contributions

Madhav Dobhal: writing – original draft, formal analysis, data curation; Aditya Sharma: writing – review & editing, conceptualization, project administration, resources, supervision; Bhavi Agrawal: formal analysis, data curation; Mayora Varshney: formal analysis, resources, data curation; Hyun-Joon Shin: writing – review & editing, resources; Ranjeet Kumar Brajpuriya: writing – review & editing, resources, project administration; Shalendra Kumar: writing – review & editing, resources, project administration.

Conflicts of interest

No known conflicting financial interests or personal ties that might have influenced the work described in this paper are disclosed by any of the authors.

Data availability

The data used to support the findings of this study are included in the article and supplementary information (SI). Raw data that support the findings of this study are available from the corresponding author, upon reasonable request.

Supplementary information is available. See DOI: https://doi.org/10.1039/d6na00014b.

Acknowledgements

The authors (Aditya Sharma, Shalendra Kumar, and Ranjeet Kumar Brajpuriya) are thankful to UPES, Dehradun, for providing experimental facilities at the Central Instrumentation Centre (CIC). Madhav Dobhal is thankful to R&D UPES, Dehradun, for offering a research fellowship. H.J. Shin would like to acknowledge the support from the RS-2024-00358571 and 2022-00143178 programs funded by the National Research Foundation (NRF), Korea, and the support from the IITP-RS-2024-00437284 program under ITRC, IITP, funded by the Ministry

of Science and ICT (MIST), Korea. Aditya Sharma, Shalendra Kumar, and Ranjeet Kumar Brajpuriya are thankful to the Uttarakhand State Council for Science and Technology (UCOST, Dehradun) for financial support under the R&D project scheme (UCOST-RND-39/2024-UCOST-DPT/26805).

Notes and references

1 O. Gerard, A. Numan, S. Krishnan, M. Khalid, R. Subramaniam and R. Kasi, *J. Energy Storage*, 2022, **50**, 104283.
2 J. Iqbal, A. Numan, S. Rafique, R. Jafer, S. Mohamad, K. Ramesh and S. Ramesh, *Electrochim. Acta*, 2018, **278**, 72–82.
3 I. Shaheen, I. Hussain, T. Zahra, M. S. Javed, S. S. A. Shah, K. Khan, M. B. Hanif, M. A. Assiri, Z. Said, W. U. Arifeen, B. Akkinepally and K. Zhang, *J. Energy Storage*, 2023, **72**, 108719.
4 C. Gao, J. Huang, Y. Xiao, G. Zhang, C. Dai, Z. Li, Y. Zhao, L. Jiang and L. Qu, *Nat. Commun.*, 2021, **12**, 2647.
5 D. A. Cullen, K. C. Neyerlin, R. K. Ahluwalia, R. Mukundan, K. L. More, R. L. Borup, A. Z. Weber, D. J. Myers and A. Kusoglu, *Nat. Energy*, 2021, **6**, 462–474.
6 N. A. Sepulveda, J. D. Jenkins, A. Edington, D. S. Mallapragada and R. K. Lester, *Nat. Energy*, 2021, **6**, 506–516.
7 D. M. Davies, M. G. Verde, O. Mnyshenko, Y. R. Chen, R. Rajeev, Y. S. Meng and G. Elliott, *Nat. Energy*, 2018, **4**, 42–50.
8 T. M. Gür, *Energy Environ. Sci.*, 2018, **11**, 2696–2767.
9 S. Dhibar, in *Hybrid Polymer Composite Materials*, Elsevier, 2017, pp. 211–248.
10 Y. B. Pottathara, H. R. Tiyyagura, Z. Ahmad and K. K. Sadasivuni, *J. Energy Storage*, 2020, **30**, 101549.
11 Z. Bo, X. Lu, H. Yang, S. Wu, X. Cheng, B. Gong, Z. Huang, J. Yan, K. Cen and K. Ostrikov, *J. Energy Storage*, 2021, **42**, 103084.
12 A. M. Teli, S. A. Beknalkar, V. V. Satale, M. A. Yewale, R. U. Amate, P. J. Morankar, J. C. Shin and H. H. Kim, *J. Alloys Compd.*, 2024, **1005**, 175950.
13 L. L. Zhang and X. S. Zhao, *Chem. Soc. Rev.*, 2009, **38**, 2520.
14 C. V. V. Muralee Gopi, R. Vinodh, S. Sambasivam, I. M. Obaidat and H.-J. Kim, *J. Energy Storage*, 2020, **27**, 101035.
15 H. Li, Z. Tang, Z. Liu and C. Zhi, *Joule*, 2019, **3**, 613–619.
16 H. H. Hegazy, J. Khan, N. Shakeel, E. A. Alabdullkarem, M. I. Saleem, H. Alrobei and I. S. Yahia, *RSC Adv.*, 2024, **14**, 32958–32977.
17 S. Angizi, S. A. A. Alem and A. Pakdel, *Energies*, 2022, **15**, 1162.
18 J. Khan, A. Ahmed, M. I. Saleem and A. A. Al-Kahtani, *Sustainable Energy Fuels*, 2024, **8**, 4355–4364.
19 F. Bibi, I. A. Soomro, A. Hanan, M. N. Lakhan, A. Khan, N. R. Goraya, Z. U. Rehman, I. Hussain and K. Zhang, *J. Mater. Sci. Technol.*, 2024, **202**, 82–118.
20 B. Matović, J. Luković, M. Nikolić, B. Babić, N. Stanković, B. Jokić and B. Jelenković, *Ceram. Int.*, 2016, **42**, 16655–16658.
21 H. N. Mutua, D. J. Tarimo, G. Rutavi, V. Maphiri, J. Mwabora, R. Musembi and N. Manyala, *J. Energy Storage*, 2025, **107**, 114968.
22 D. Krishnamoorthy and A. K. Singh, *Diamond Relat. Mater.*, 2025, **152**, 111976.
23 G. Maheshwaran, M. R. Prabhu, G. Ravi, K. Sankaranarayanan and S. Sudhahar, *Nano Energy*, 2023, **106**, 108060.
24 T. Li, X. Jiao, T. You, F. Dai, P. Zhang, F. Yu, L. Hu, L. Ding, L. Zhang, Z. Wen and Y. Wu, *Ceram. Int.*, 2019, **45**, 4283–4289.
25 C. K. Maity, G. Hatui, S. Sahoo, P. Saren and G. C. Nayak, *ChemistrySelect*, 2019, **4**, 3672–3680.
26 K. Dhamodharan and A. K. Singh, *J. Alloys Compd.*, 2024, **997**, 174732.
27 N. Prabhakar, M. Lakshmi Narayanan, H. Mana-ay, N. Ponpandian, C. Viswanathan and P.-Y. Chen, *Fuel*, 2025, **398**, 135489.
28 A. E. Naclerio and P. R. Kidambi, *Adv. Mater.*, 2023, **35**(6), 2207374.
29 S. Chahal, L. Phor, S. Singh, A. Singh, J. Malik, P. Goel, A. Kumar, S. Kumar, Ankita and P. Kumar, *Ceram. Int.*, 2022, **48**, 28961–28968.
30 Ankita, S. Chahal, S. Singh, Suman, K. K. H. De Silva, A. Kumar, S. Kumar, L. Kumar, M. Yoshimura, R. Kumar and P. Kumar, *Vacuum*, 2023, **215**, 112280.
31 M. Mirzaee, A. Rashidi, A. Zolriasatein and M. Rezaei Abadchi, *Ceram. Int.*, 2021, **47**, 5977–5984.
32 S. Kumar, F. Ahmed, N. Ahmad, N. M. Shaalan, R. Kumar, A. Alshoaibi, N. Arshi, S. Dalela, M. Albossed, K. H. Chae, P. A. Alvi and K. Kumari, *Materials*, 2022, **15**, 4118.
33 S. Kumar, F. Ahmed, N. M. Shaalan, N. Arshi, S. Dalela and K. H. Chae, *Materials*, 2023, **16**, 4328.
34 N. K. Gautam, A. Sharma, M. Varshney, J. P. Singh, H.-J. Shin, S. Kumar, R. Brajpuriya, B. Lee, K.-H. Chae and S.-O. Won, *New J. Chem.*, 2025, **49**, 11203–11217.
35 C. Tang, Y. Bando, Y. Huang, C. Zhi and D. Golberg, *Adv. Funct. Mater.*, 2008, **18**, 3653–3661.
36 N. Chalmpes, A. B. Bourlinos, A. W. Alsmaeil, A. S. Aljarrah, C. E. Salmas, M. A. Karakassides and E. P. Giannelis, *Mater. Res. Express*, 2024, **11**, 035002.
37 L. J. Berchmans, B. Bharathi, K. Amalajyothi and K. Subramanian, *Int. J. Self-Propag. High-Temp. Synth.*, 2009, **18**, 34–37.
38 T. Shen, S. Liu, W. Yan and J. Wang, *J. Mater. Sci.*, 2019, **54**, 8852–8859.
39 S. A. Idrees, L. A. Jamil and K. M. Omer, *RSC Adv.*, 2023, **13**, 6779–6792.
40 N. G. Doménech, Á. Coogan, F. Purcell-Milton, M. L. Casasín García, A. S. Arjona, M. B. Cabré, A. Rafferty, K. McKelvey, P. Dunne and Y. K. Gun'ko, *Nanoscale Adv.*, 2022, **4**, 4895–4904.
41 A. Sunny, A. Balapure, R. Ganesan and R. Thamankar, *ACS Omega*, 2022, **7**, 33926–33933.

42 A. Kumar, G. Malik, S. Sharma, R. Chandra and R. S. Mulik, *Ceram. Int.*, 2021, **47**, 30985–30992.
43 A. Kumar, G. Malik, K. Goyal, N. Sardana, R. Chandra and R. S. Mulik, *Vacuum*, 2021, **184**, 109927; M. H. Khan, H. K. Liu, X. Sun, Y. Yamauchi, Y. Bando, D. Golberg and Z. Huang, *Mater. Today*, 2017, **20**(10), 611–628.
44 R. Singh, G. Kalita, R. D. Mahyavanshi, S. Adhikari, H. Uchida, M. Tanemura, M. Umeno and T. Kawahara, *AIP Adv.*, 2019, **9**(3), 035043.
45 C. Sharma, P. Vanishree, B. Rani, N. Lohia, G. Swati, R. Srivastava and S. N. Sharma, *Electrochim. Acta*, 2023, **463**, 142848.
46 J. I. Langford, D. Louër and P. Scardi, *J. Appl. Crystallogr.*, 2000, **33**, 964–974.
47 J. Qu, Q. Li, C. Luo, J. Cheng and X. Hou, *Coatings*, 2018, **8**, 214.
48 M. Nasit, K. Kumari, N. Yadav, B.-H. Koo, S. Dalela, A. Vij, A. Sharma, P. A. Alvi and S. Kumar, *J. Phys. Chem. Solids*, 2026, **208**, 113117.
49 G. R. Reddy, G. R. Dillip, G. L. Manjunath and S. W. Joo, *J. Electrochem. Soc.*, 2022, **169**, 060549.
50 X. Zhang, H. Liao, X. Liu, R. Shang, Y. Zhou and Y. Zhou, *Ionics*, 2020, **26**, 3599–3607.
51 G. Dhiman, K. Kumari, S. Dalela, F. Ahmed, N. M. Shaalan, P. A. Alvi, R. K. Brajpuriya and S. Kumar, *J. Energy Storage*, 2025, **106**, 114743.
52 G. Rajasekhara Reddy, N. Siva Kumar, B. Deva Prasad Raju, G. Shanmugam, E. H. Al-Ghurabi and M. Asif, *Nanomaterials*, 2020, **10**, 1206.
53 G. R. Reddy, B. Sravani, N. Jung, G. R. Dillip and S. W. Joo, *ACS Appl. Mater. Interfaces*, 2023, **15**, 36500–36511.
54 G. Rajasekhara Reddy, N. Ramesh Reddy, G. R. Dillip and S. W. Joo, *Energy Fuels*, 2022, **36**, 5965–5978.
55 M. Nasit, A. Vij, K. Kumari, B.-H. Koo, S. Dalela, P. A. Alvi, R. K. Brajpuriya and S. Kumar, *J. Alloys Compd.*, 2025, **1013**, 178428.
56 K. Sunil Kumar, J. Pundareekam Goud, N. Roy, K. Jong Su and S. W. Joo, *Ceram. Int.*, 2024, **50**, 20535–20546.
57 V. Shanmugapriya, S. Arunpandiyan, G. Hariharan, S. Bharathi, B. Selvakumar and A. Arivarasan, *J. Alloys Compd.*, 2023, **935**, 167994.
58 X. Zheng, G. Wang, F. Huang, H. Liu, C. Gong, S. Wen, Y. Hu, G. Zheng and D. Chen, *Front. Chem.*, 2019, **7**, 544.